Low-Loss Impedance-Matched Optical Metamaterials with Zero-Phase Delay

Seokho Yun,[†] Zhi Hao Jiang,[†] Qian Xu, Zhiwen Liu, Douglas H. Werner,[*] and Theresa S. Mayer[*]

Department of Electrical Engineering, The Pennsylvania State University, University Park, Pennsylvania 16802, United States. [†]These authors contributed equally to this work.

ABSTRACT

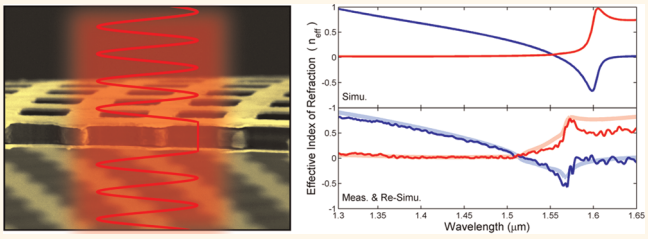

Metamaterials have dramatically expanded the range of available optical properties, enabling an array of new devices such as superlenses, perfect absorbers, and ultrafast switches. Most research has focused on demonstrating negative- and high-index metamaterials at terahertz and optical wavelengths. However, far less emphasis has been placed on low-loss near-zero-index metamaterials that exhibit unique properties including quasi-infinite phase velocity and infinite wavelength. Here, we experimentally demonstrate a free-standing metallodielectric fishnet nanostructure that has polarization-insensitive, zero-index properties with nearly ideal transmission at 1.55 μm. This goal was achieved by optimizing the metamaterial geometry to allow both its effective permittivity and permeability to approach zero together, which simultaneously produces a zero index and matched impedance to free space. The ability to design and fabricate low-loss, near-zero-index optical metamaterials is essential for new devices such as beam collimators, zero-phase delay lines, and transformation optics lenses.

KEYWORDS: optical metamaterial · zero/low-index · zero-phase delay · impedance-matched · free-standing

Metamaterials provide a unique opportunity to create highly customizable refractive index-engineered thin films that will enable optical devices with entirely new physical properties, optical functions, and form factors. By optimizing the geometry of artificially engineered metallodielectric nanostructures to give a specific electric and magnetic response to incident electromagnetic waves, the effective refractive index of the composite materials can be varied from negative,[1−5] through zero,[6−9] to large positive values.[10] Negative-index metamaterials (NIMs) have been the subject of intense investigation since Pendry's proposal of a flat NIM lens with sub-diffraction-limited resolution.[5] However, far less research has focused on the equally important class of low- and zero-index metamaterials (LIMs/ZIMs), which provide quasi-infinite phase velocity and infinite wavelength for the light propagating inside.[11,12] These optical properties can be exploited to produce a variety of new and exciting electromagnetic devices with unique functionalities, including electromagnetic cloaks,[11,13] beam self-collimators,[14] flat far-field focusing lenses,[7,15,16] low-index mirrors,[6] electromangnetic field enhancers,[17] and compact zero-phase delay lines.[18]

Along with providing the required low-to-zero refractive index values, many metamaterial-enabled devices must have nearly ideal optical transmission, with minimal reflection and absorption loss. To minimize reflection loss, the interfacial impedance of the metamaterial should be well matched to the impedance of its surroundings. The effective refractive index (n_{eff}) and interfacial impedance values (Z_{eff}) of a metamaterial are given by

$$n_{eff} = \sqrt{\varepsilon_{eff}\mu_{eff}},\ Z_{eff} = \sqrt{\mu_{eff}/\varepsilon_{eff}} \quad (1)$$

where ε_{eff} and μ_{eff} are its effective permittivity and permeability, respectively. Consequently, the metallodielectric nanostructures must be optimized to give an electromagnetic response that simultaneously balances $\varepsilon_{eff}\mu_{eff}$ and $\mu_{eff}/\varepsilon_{eff}$ to produce the desired refractive index and impedance match across the wavelength band of interest.

Earlier experiments on optical metamaterials primarily investigated structures with specific negative-index or high-index values but with uncontrolled interfacial impedance. For most device applications, the metamaterial structures must have nearly ideal optical transmission with minimal reflection and absorption loss. In the zero-to-low-index regime, it has been shown theoretically that the low ε_{eff} produced by volumetric wire arrays[6] or wire meshes[7] yield metamaterials with low n_{eff}. A low index can

* Address correspondence to tsm2@psu.edu, dhw@psu.edu.

Received for review March 20, 2012 and accepted April 24, 2012.

Published online April 24, 2012
10.1021/nn3012338

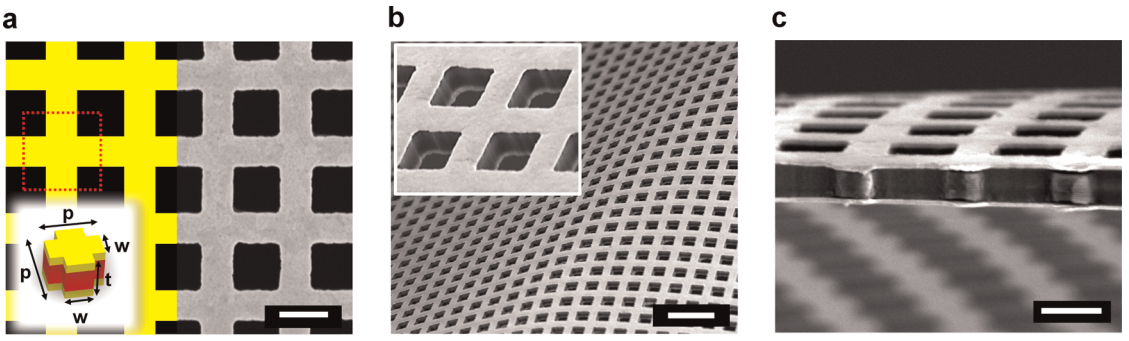

Figure 1. Schematic of a zero-index metamaterial and FESEM images of the fabricated device. (a) Left: Diagram of the optimized fishnet structure that produces a near zero refractive index at 1.55 μm. One unit cell is enclosed within the red dotted square. The inset shows a 3D view of the unit cell with $w = 365$ nm, $p = 956$ nm, and $t = 381$ nm. The top and bottom Au layers (yellow) are 39 nm thick, and the polyimide layer (red) is 303 nm thick. Right: Top-view FESEM image of the fabricated ZIM. Scale bar, 500 nm. (b) FESEM image of the free-standing, flexible ZIM structure. Scale bar, 2 μm. (c) Cross-sectional FESEM image showing the Au and polyimide layers. Scale bar, 500 nm.

also be created using artificial magnetic resonators with near zero μ_{eff}.[8] Because the low index is obtained by manipulating only one of the effective medium parameters (ε_{eff} or μ_{eff}), the interfacial impedance is limited to either $Z_{eff} \to \infty$ or $Z_{eff} \to 0$ and cannot be easily tailored to match the impedance of surrounding layers. For example, if the metamaterial structure is surrounded by air, its effective impedance should be matched to that of free space,[9,16] which is given by

$$Z_{eff} = Z_0 = \sqrt{\mu_0/\varepsilon_0} \quad (2)$$

where ε_0 is the permittivity and μ_0 is the permeability of free space. This condition can only be satisfied by tailoring both the ε_{eff} and the μ_{eff} of the metamaterial structure.

In this paper, we demonstrate a polarization-insensitive optical ZIM with a nearly perfect transmission fabricated in the form of a mechanically flexible, free-standing thin film. This was achieved by optimizing the geometry of the metallodielectric fishnet structure to give $\varepsilon_{eff} \to 0$ and $\mu_{eff} \to 0$ at a wavelength of 1.55 μm, which provides a matched impedance with free space ($Z_{eff}/Z_0 \approx 1$). The nanofabricated ZIM samples accurately replicated the optimized, axially symmetric fishnet design, thereby minimizing degradation in optical properties (increased loss) due to bianisotropy from substrate loading[19] and/or from feature asymmetry.[20] The experimentally retrieved effective medium parameters obtained by inverting the complete set of scattering parameters (amplitude and phase) measured using spectral holography confirmed the targeted design properties, giving an $n_{eff} = 0.121 + 0.032i$ and $Z_{eff}/Z_0 = 0.861 - 0.049i$.

RESULTS AND DISCUSSION

Electromagnetic Design Optimization. The impedance-matched metamaterial with a near-zero-index band at 1.55 μm was designed using a free-standing symmetric fishnet nanostructure consisting of two gold (Au) screens separated by a polyimide spacer with square air holes perforating all three layers (see Figure 1a). The air holes were aligned in a doubly periodic arrangement with identical periodicity in both the *x*- and *y*-directions, thus making the structure polarization insensitive to incoming light at normal incidence. With the combination of the resonant magnetic paired strips and nonresonant electric strips, the fishnet structure can be regarded as being composed of an array of magnetic dipoles embedded inside a diluted metal, which yields a resonant μ_{eff} and a Drude-like ε_{eff}. By carefully tailoring the nanostructure geometry to give $\mu_{eff} \to 0$ and $\varepsilon_{eff} \to 0$ at the same wavelength, the desired impedance-matched ZIM can be obtained.

Due to the challenging design criteria for an impedance-matched ZIM, a powerful stochastic genetic algorithm (GA)[21] technique was employed to optimize the fishnet nanostructure to satisfy the performance goals—a near-zero effective refractive index and an impedance matched to free space. The optimizer determined the geometric dimensions of the fishnet, including the unit cell size, air hole size, and layer thicknesses, to provide optical properties that best satisfied the design criteria. The measured optical properties of the constituent materials (*i.e.*, Au and polyimide) and the applicable nanofabrication constraints were incorporated into the optimizer to accurately model the material dispersion and to ensure that the resulting structure could be readily fabricated without further modification. In the numerical simulations, Au was modeled as a dispersive dielectric with complex permittivity that was determined by spectroscopic ellipsometry measurements of the deposited films. For each candidate design in the GA optimization, the complex transmission and reflection coefficients were predicted using a full-wave periodic finite-element boundary-integral (PFEBI) solver.[22] The effective refractive index (n_{eff}) and normalized effective

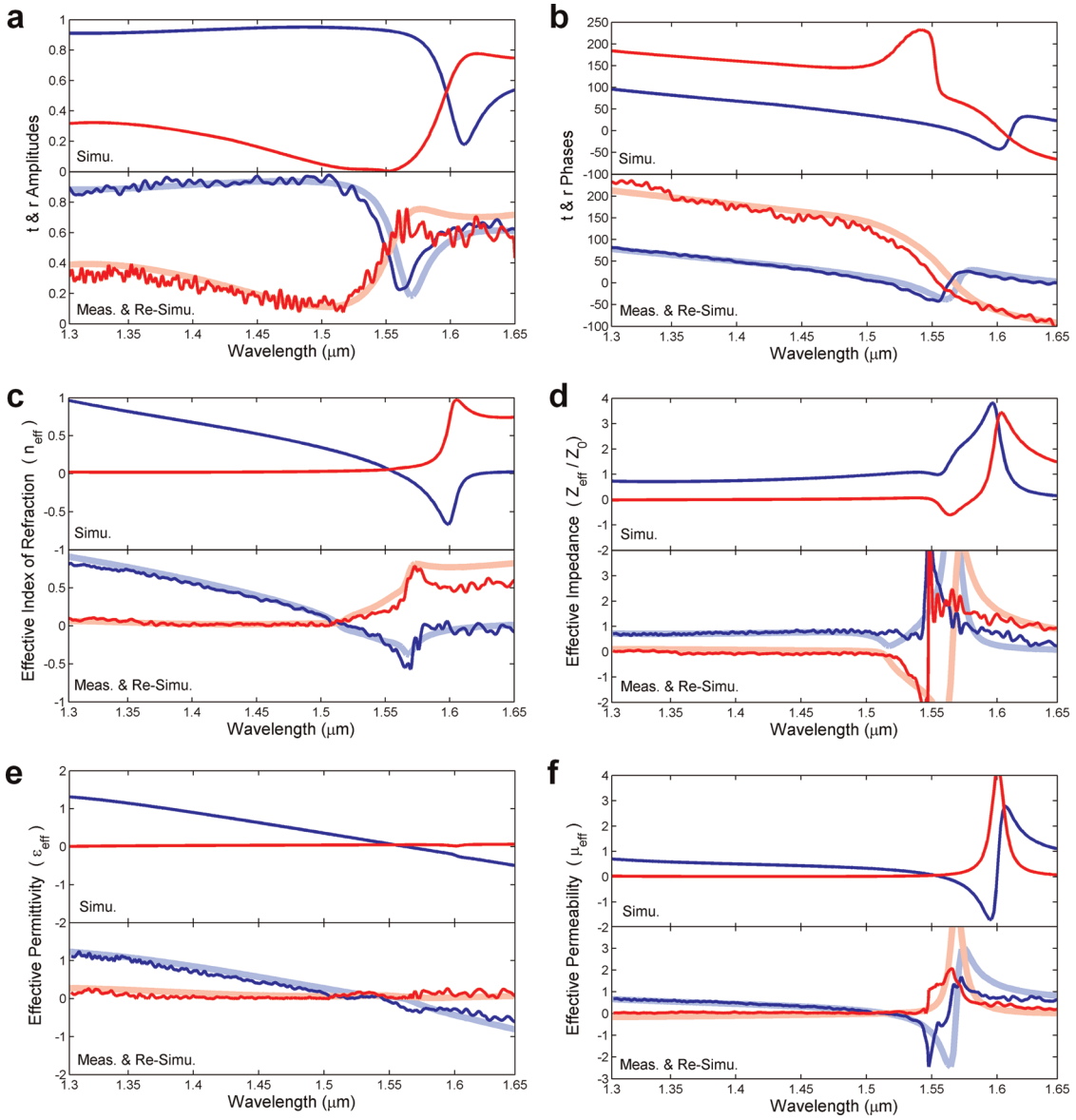

Figure 2. Simulated and measured complex transmission and reflection coefficients validate the predicted zero-index metamaterial properties of the fishnet nanostructure. Amplitude (a) and phase (b) of the transmission (blue, light blue (resimulated with adjusted dimensions)) and reflection (red, light red (resimulated with adjusted dimensions)) coefficients. A high transmission amplitude and near-zero-phase delay is observed at 1.55 and 1.5 μm for both the simulated and the measured ZIM structures. Real (blue, light blue (resimulated with adjusted dimensions)) and imaginary (red, light red (resimulated with adjusted dimensions)) parts of the inverted effective refractive index (c) and normalized effective impedance (d). The nanofabricated fishnet structure has a near-zero refractive index and a near-unity normalized effective impedance with extremely small imaginary parts at 1.5 μm. Real (blue, light blue (resimulated with adjusted dimensions)) and imaginary (red, light red (resimulated with adjusted dimensions)) parts of the inverted effective permittivity (e) and effective permeability (f). The measured structure has a near-zero permittivity and a near-zero permeability with negligible imaginary parts at 1.5 μm.

impedance (Z_{eff}/Z_0) were then inverted from the scattering parameters using an established retrieval method[23−25] and compared with an ideal ZIM response to determine the candidate's cost defined by

$$\text{cost} = |n_{eff} - n_{tar}|^2 + |Z_{eff}/Z_0 - Z_{tar}/Z_0|^2 \quad (3)$$

where $n_{tar} = 0 + 0i$ and $Z_{tar}/Z_0 = 1 + 0i$ are the target effective refractive index and normalized effective impedance, respectively. The GA minimized the cost and evolved a ZIM structure with a cost (deviation) of only 0.008 from the design criteria specified in eq 3.

Symmetric Fishnet for Zero-Phase Delay. The geometry and dimensions of the optimized ZIM design are shown in Figure 1a. The width and length of the three-layered crossed strips in the unit cell are 365 and 956 nm, respectively. A 303 nm thick polyimide layer separates the 39 nm thick top and bottom Au screen layers. The predicted transmission and reflection coefficients of this GA-optimized fishnet nanostructure

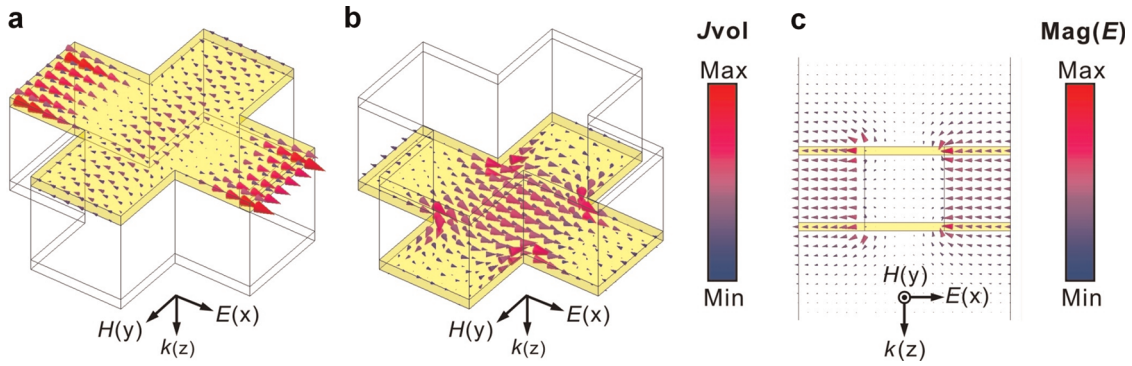

Figure 3. Numerical simulations of current distribution on the Au screens in the zero-index band. Distribution of volumetric current density on the top (a) and bottom (b) Au layers of the ZIM excited with a normally incident beam having the polarization shown. The antiparallel currents induced by the incident magnetic field create the resonant magnetic response in the three-layer fishnet structure. (c) Cross-sectional view of a snapshot of the electric field. The nearly identical field vectors throughout the fishnet structure confirm that the metamaterial has a near-zero-phase delay with high transmission.

are shown in Figure 2a,b. Because the effective impedance is well-matched to free space and the absorption loss in the metamaterial is low, the transmission amplitude remains remarkably high at ~95% around the target ZIM band at 1.55 μm. In addition, the transmission phase is in the vicinity of zero degrees and possesses a positive value (which is required, *e.g.*, in cloaking devices),[9,26,27] indicating a near-zero-phase delay as a normally incident wave travels through the metamaterial. Considering the physical thickness of the structure, which is approximately $\lambda/4$, this near-zero absolute transmission phase provides confirmation that a near-zero optical path length can be achieved using this metamaterial.

The inverted theoretical effective material parameters are shown in Figure 2c,d. A zero-index band with an extremely small extinction coefficient ($n_{eff} = 0.072 + 0.051i$), which is indicative of the low absorption losses in the structure, is observed exactly at 1.55 μm. The near-unity normalized effective impedance with small imaginary part ($Z_{eff}/Z_0 = 1.009 - 0.021i$) substantiates the low reflection loss as exhibited in the transmission and reflection amplitudes. To quantitatively evaluate the ZIM performance, two figures-of-merit (FOMs) are defined for the zero-index band:

$$\mathrm{FOM}_n = 1/|n_{eff}|,\ \mathrm{FOM}_Z = 1/|Z_{eff}/Z_0 - 1| \quad (4)$$

where FOM_n evaluates how closely the effective refractive index approaches zero, and FOM_Z evaluates how closely the normalized effective impedance approaches unity. For this specific optimized design, the achieved FOMs have high values of 11.3 and 43.8, respectively. This represents a new benchmark in the state-of-the-art for optical ZIMs.

Electromagnetic Properties. To acquire a clear understanding of the optical response of this ZIM, the current distributions on the top and bottom Au layers at a wavelength of 1.55 μm are plotted in Figure 3a,b with an incident electric field linearly polarized along the *x*-direction. The array of long Au metal strips, which is aligned to the *x*-axis along the incident electric field, provides a diluted Drude-type response (see Figure 2e).[28] The antiparallel currents induced by the incident magnetic field along the *y*-axis produce a resonant magnetic response, resulting in a Lorentzian line-shaped resonance in the effective permeability (see Figure 2f).[29] In this design, the geometry of the fishnet was optimized to give near-zero values of $\varepsilon_{eff} = 0.068 + 0.051i$ and $\mu_{eff} = 0.072 + 0.049i$ at 1.55 μm, leading to a low-loss, impedance-matched ZIM (see Figure 2c,d). The near-zero-phase delay of this ZIM is clearly shown in the snapshot of the field evolution in Figure 3c. Specifically, the amplitude and phase of the electric fields are nearly identical on the top and bottom interfaces as well as everywhere inside the metamaterial.

Nanofabrication. The optimized low-loss ZIM properties are only valid for an ideal symmetric nanostructure, which has air holes with perfectly vertical (90°) sidewalls and is surrounded by air on the top and bottom surfaces. Previously reported fishnet-based optical metamaterials[1,3,4,20] were fabricated by defining the nanometer scale air holes in multilayer metal/dielectric stacks deposited on optically transparent substrates using either focused ion beam (FIB) etching[1] or lift-off techniques.[3,4,20] These structures suffer from process-induced nonidealities that degrade their optical properties. Specifically, the physical FIB etching process causes the air holes in the topmost stack layers to widen and the sputtered materials to redeposit onto the etched sidewalls.[1] The lift-off process limits the sidewall angle to <80° for multilayer stacks that are in the range of 100−300 nm thick.[20] The slight deviation in the sidewall angle of 10° from vertical leads to asymmetry that introduces coupling between the electric and magnetic fields which is not present in the symmetric fishnet structure.[20] As presented in the Supporting Information, S1, this coupling would result in a significant decrease in the transmission amplitude from 95 to 77% in the optimized ZIM structure

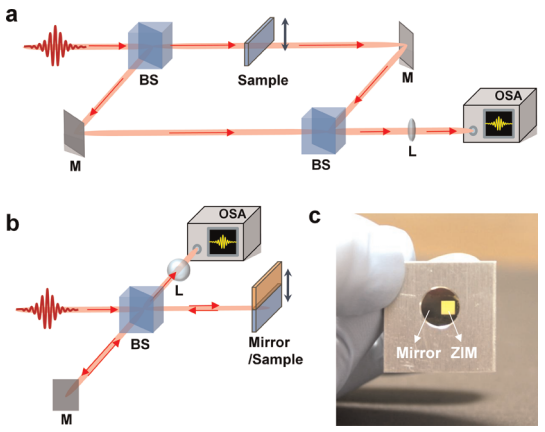

Figure 4. Optical characterization of the free-standing fishnet nanostructure. (a) Schematic of the Mach–Zehnder interferometer used to find the complex transmission coefficients of the ZIM. (b) Schematic of the Michelson interferometer used to find the complex reflection coefficients of the ZIM. M, mirror; L, lens; BS, beam splitter; OSA, optical spectrum analyzer. (c) Photograph of the 3 mm × 3 mm fishnet structure (yellow) and reference mirror (black) mounted on an Al frame for optical characterization.

(see Figure S2). This underscores the importance of fabricating nanostructures that approach the ideal designed geometry to experimentally realize the theoretically predicted properties.

In this work, a top-down nanofabrication process that employed high-aspect-ratio dry etching to form air holes in the thick metal/dielectric/metal stack was developed to overcome the inherent limitations of the FIB and lift-off processes. The optimized ZIM design was made by first sequentially depositing the three-layer stack using electron-beam evaporation and spin-coating for the Au and polyimide layers, respectively. The individual evaporation, coating, and thermal treatment steps were optimized to produce films with high optical quality (see Methods).[30] To create the fishnet nanostructure, a sacrificial silicon dioxide (SiO_2) hard etch mask was added on top of the Au–polyimide–Au stack using low-temperature plasma-enhanced chemical vapor deposition (PECVD), and the air hole array pattern was defined in the hard mask using electron-beam lithography and fluorine-based reactive ion etching (RIE). This pattern was transferred through the Au and the polyimide layers by anisotropic dry etching using an inductively coupled chlorine-based high-density plasma process. In the final step, the SiO_2 hard mask was removed by low-power dry etching, and the Au–polyimide–Au fishnet structure was released from the Si handle substrate to give the symmetric ZIM structure.

Figure 1 shows field-emission scanning electron microscope (FESEM) images of the fabricated fishnet structure. These images demonstrate that this process accurately reproduced the optimized ZIM design with air hole dimensions of 590 nm × 590 nm (measured on top and backside), nearly ideal vertical sidewalls (>89°), and no visible redeposition of Au on the etched polyimide sidewalls. Additionally, because the constituent Au and polyimide materials are ductile, the free-standing fishnet structure is flexible and can be deformed without fracturing. As shown in Figure 4c, the symmetric ZIM was mounted on an aluminum frame for optical characterization. The topmost Au layer present in the areas surrounding the ZIM was used as a reference mirror for reflection measurements.

Optical Characterization. The zero-index properties of the nanofabricated fishnet structure were verified by experimentally measuring the amplitude and phase of the transmission and reflection coefficients using a spectral holography technique.[31,32] First, transmission measurements were made using a Mach–Zehnder interferometer with a white-light supercontinuum input source (see Figure 4a, solid red). Interferograms were collected over a broad range of wavelengths from 1.2 to 1.7 μm before and after inserting the free-standing ZIM in one of the two optical beam paths. The complex transmission coefficient t of the ZIM was calculated by taking the ratio of the reconstructed signal terms of the two measurements (see Figure S1). Next, reflection measurements were made on the same sample using a Michelson interferometer (see Figure 4b, solid blue). Interferograms were collected for the ZIM as well as the adjacent reference mirror, and the complex reflection coefficient r was determined from the ratio of their reconstructed signals (see Figure S2).

The measured transmission and reflection coefficients are compared to the simulated values in Figure 2a,b. The distinguishing spectral features present in simulation are blue-shifted by 50 nm in the fabricated structure, and the prominent increase in the simulated reflection phase near the designed resonance is missing. Despite these differences, the average values of measured transmission and reflection amplitude remain above 95% and below 18% within the zero-index band around 1.50 μm. In addition, the transmission phase passes through zero at 1.50 μm, which results in a near-zero optical path length, that is, quasi-infinite phase velocity. This confirms that the fabricated ZIM has a nearly ideal impedance match to free space (low reflection loss) and has a low absorption loss with the desired near-zero-index value.

To explain the small discrepancies between experiment and theory, the optical properties of the ZIM structure were resimulated with several different polyimide layer thicknesses around the optimized values. This analysis revealed that the best agreement is obtained for a structure having a slightly thicker polyimide layer of 321 nm, which is within the ~10% variation in polyimide layer thicknesses measured on a series of planar test samples. As shown in Figure 2a,b,

all of the simulated transmission and reflection coefficient features now match the measured values and have negligible shift over the entire wavelength range. This further demonstrates that the impedance-matched condition of this fishnet structure is robust against small variations in dielectric thickness because the infinite wavelength in the zero-index band is preserved. This is in sharp contrast to the strong dependence on air hole sidewall angle, which resulted in a significant decrease in transmission amplitude.

The effective medium properties of the fabricated ZIM that were retrieved using the measured transmission and reflection coefficients are plotted in Figure 2b–e. As expected from simulation, the real and imaginary parts of ε_{eff} and μ_{eff} are close to zero within the zero-index band of the structure. The dielectric properties give a complex effective refractive index of $n_{eff} = 0.121 + 0.032i$ and a normalized effective impedance of $Z_{eff}/Z_0 = 0.861 - 0.049i$ at the zero-phase crossing wavelength of 1.50 μm. These values agree well with the target design values of $n_{eff} = 0.072 + 0.051i$ and $Z_{eff}/Z_0 = 1.009 - 0.021$i and give a measured $FOM_n = 8.1$ and $FOM_Z = 17.2$ for this structure. The measured data verify theory and show that high-performance optical metamaterials can be experimentally realized with proper control over the nanofabrication process.

CONCLUSIONS

In summary, a polarization-insensitive, impedance-matched ZIM with nearly perfect transmission at optical wavelengths was designed, fabricated, and characterized. This was achieved by optimizing a metallodielectic fishnet structure to simultaneously balance the electric and magnetic response to give $\varepsilon_{eff} \to 0$ and $\mu_{eff} \to 0$ at a wavelength of 1.55 μm, which resulted in $n_{eff} \sim 0$ and $Z_{eff}/Z_0 \sim 1$. The nanofabricated free-standing, Au–polyimide–Au ZIM accurately reproduced the designed geometry and provided an axially symmetric structure that eliminated bianisotropy-induced degradation in optical properties. Measurements of the complex transmission and reflection coefficients acquired using spectral holography agreed well with the theoretical predictions and verified the near-zero-index and highly transmissive properties of the fabricated metamaterial. This demonstration of a low-loss ZIM paves the way to more advanced metamaterial-enabled devices that require a range of low-index values (*e.g.*, $0 \leq n_{eff} \leq 1$).

METHODS

Nanofabrication of the ZIM Structure. The process began by depositing the three-layer metallodielectric stack on a thermally oxidized Si substrate, which served as a sacrificial handle wafer during fabrication. The bottom 39 nm thick Au layer was electron-beam-evaporated (Kurt Lesker LAB-18) onto the handle wafer at a rate of 1 Å/s and at a substrate temperature of 25 °C. This process produced a smooth and continuous Au film with a 0.8 nm rms roughness as measured by atomic force microscopy. The optical constants of the Au film used in numerical simulations were determined from spectroscopic ellipsometry (SE) measurements over the wavelength range of 300 nm to 33 μm (J. A. Woollam VASE-160 and IR-VASE). The intermediate polyimide dielectric layer was then deposited by spin-coating the polyimide precursor (HD Microsystem PI2556 resin diluted by 50% with HD Microsystem T9039 thinner) onto the Au film at 2400 rpm for 40 s. The film was imidized by heating the sample at 150 °C for 30 min and then at 250 °C for 2 h in a nitrogen-purged convection oven. The polyimide optical constants used in the numerical simulations were determined from SE measurements (300 nm to 33 μm) of films deposited on bare fused silica or Si substrates. During ZIM structure fabrication, additional polyimide films deposited on separate Au-coated test samples were also calibrated by SE measurements, and the polyimide layer thicknesses were consistently found to be within 10% of the target value of 303 nm. The top 39 nm thick Au layer was electron-beam-evaporated using the same conditions as the bottom Au layer. Finally, plasma-enhanced chemical vapor deposition (Applied Materials P-5000 PECVD Cluster) was used to add a 200 nm thick SiO_2 hard mask layer on top of the stack. The process temperature was maintained at 150 °C to minimize changes in the optical properties of the Au and polyimide layers.

The optimized fishnet structure was defined by electron-beam lithography and reactive ion etching. A 300 nm thick layer of positive electron-beam resist (ZEON ZEP 520A) was applied by spin-coating at 5000 rpm for 1 min and soft-baking at 180 °C for 3 min. A 3 mm × 3 mm array of the 591 nm × 591 nm square air holes was patterned by exposing the resist at a dose of 180 μC/cm^2, developing the resist in *n*-amyl acetate for 3 min, and rinsing the sample in methyl isobutyl ketone and isopropyl alcohol (8:1) for 1 min. The lithographically defined pattern was transferred into the SiO_2 layer by dry etching in an inductively coupled plasma (ICP) RIE system (Trion Technologies Orion) using CF_3 (35 sccm) and O_2 (5 sccm) at a pressure of 20 mTorr, a substrate power of 100 W, and an ICP power of 50 W. Using the SiO_2 layer as a hard mask, the top and bottom Au layers were etched in the same system using Cl_2 (35 sccm) and Ar (5 sccm) at a pressure of 20 mTorr, a substrate power of 200 W, and an ICP power of 50 W. The polyimide layer was etched in a magnetically enhanced (ME) RIE system (Applied Materials P-5000 Cluster) with helium backside cooling using O_2 (90 sccm) at a pressure of 10 mTorr, a substrate power of 150 W, and a magnetic field of 45 G. The SiO_2 hard mask was removed using a low-power CHF_3 and CF_4 plasma. The patterning and etching process resulted in air holes with nearly vertical sidewalls and no visible redeposition of Au onto the etched polyimide surfaces.

Prior to optical characterization, the three-layer fishnet structure was released from the Si handle substrate by selectively etching the thermal oxide in diluted buffered oxide etch (BOE). The free-standing structure was mounted onto an Al frame by positioning the Au reference mirror and the ZIM within a 10 mm diameter opening in the frame (see Figure 4c).

Measuring Complex Transmission and Reflection Coefficients Using Spectral Holography[31,32]**.** The supercontinuum light source used in the Mach–Zehnder and Michelson interferometers was generated using a subnanosecond pump laser (JDS Uniphase NP-10620-100) and a highly nonlinear photonic crystal fiber (BlazePhotonics SC-5.0-1040).[33] Transmission and reflection interferograms were collected using an optical spectrum analyzer (Ando electric). The complex transmission ($t = |t|e^{i\varphi_t}$) and reflection ($r = |r|e^{i\varphi_r}$) coefficients of the free-standing ZIM structure were calculated from the measured data as follows. The transmission interferograms without (I_t) and with (I'_t) the ZIM inserted in the beam path are given by

$$I_t = |R+S|^2 = |R|^2 + |S|^2 + SR^* + RS^* \quad (5)$$

and

$$I'_t = |R + St|^2 = |R|^2 + |St|^2 + StR^* + RS^*t^* \quad (6)$$

where R and S are the respective field amplitudes of the reference beam and the signal beam in the frequency domain (see Figure S1a). The inverse Fourier transforms (IFT) of these two interferograms are shown in Figure S1b. The center peaks in each spectrum correspond to the IFT of the first two terms on the right-hand side of eqs 5 and 6, and the sideband peaks represent the IFTs of the remaining terms in these equations. In our experiments, the signal beam path length was longer than that of the reference beam path. Therefore, the sideband peaks on the right in each spectrum correspond to the SR^* and StR^* terms. The complex transmission coefficient t was obtained by taking the ratio of the Fourier transforms of the sideband peaks.

The reflection interferograms from the reference mirror (I_r) and the ZIM (I'_r) can be expressed as

$$I_r = |R + Sme^{i(\omega/c)\Delta L}|^2 = |R|^2 + |Sm|^2 + Sme^{i(\omega/c)\Delta L}R^* + RS^*m^*e^{-i(\omega/c)\Delta L} \quad (7)$$

and

$$I'_r = |R + Sr|^2 = |R|^2 + |Sr|^2 + SrR^* + RS^*r^* \quad (8)$$

where m is the mirror reflection coefficient that is approximately 1 (based on the measured value of 0.995), ΔL is the beam path length difference between the two measurements, ω is the angular frequency, and c is the speed of light. The value of ΔL was calculated by knowing that the phase difference between transmission and reflection measurements in the off-resonance long wavelength end ($\sim$1.65 μm) is $\pi/2$ (assuming the structure is lossless and possesses time reversal symmetry)[34] and was found to be $\Delta L \sim 8$ μm. The IFTs of the interferograms are shown in Figure S1d. Here, the sideband peaks on the right in each spectrum correspond to the $Sme^{i(\omega/c)\Delta L}R^*$ and SrR^* terms, and the complex reflection coefficient r was obtained by taking the ratio of the Fourier transforms of these peaks.

Conflict of Interest: The authors declare no competing financial interest.

Acknowledgment. This work was supported by the NSF MRSEC Grant No. DMR-0213623. The optimized ZIM structures were fabricated at the Penn State NSF NNIN Site.

Supporting Information Available: Simulation of fishnet structure with air holes that have sloped sidewalls (Figure S1). Transmission and reflection interferograms acquired using spectral holography (Figure S2). This material is available free of charge *via* the Internet at http://pubs.acs.org.

REFERENCES AND NOTES

1. Valentine, J.; Li, J.; Zhang, S.; Zentgraf, T.; Bartal, G.; Zhang, X. Three-Dimensional Optical Metamaterial with a Negative Refractive Index. *Nature* **2008**, *455*, 376–379.
2. Shalaev, V. M. Optical Negative-Index Metamaterials. *Nat. Photonics* **2007**, *1*, 41–48.
3. Dolling, G.; Enkrich, C.; Wegener, M.; Soukoulis, C. M.; Linden, S. Simultaneous Negative Phase and Group Velocity of Light in a Metamaterial. *Science* **2006**, *312*, 892–894.
4. Zhang, S.; Fan, W.; Panoiu, N. C.; Malloy, K. J.; Osgood, R. M.; Brueck, S. R. Experimental Demonstration of Near-Infrared Negative-Index Metamaterials. *Phys. Rev. Lett.* **2005**, *95*, 137404.
5. Pendry, J. B. Negative Refraction Makes a Perfect Lens. *Phys. Rev. Lett.* **2000**, *85*, 3966–3969.
6. Schwartz, B. T.; Piestun, R. Total External Reflection from Metamaterials with Ultralow Refractive Index. *J. Opt. Soc. Am. B* **2003**, *20*, 2448–2453.
7. Enoch, S.; Tayeb, G.; Sabouroux, P.; Guérin, N.; Vincent, P. A Metamaterial for Directive Emission. *Phys. Rev. Lett.* **2002**, *89*, 213902.
8. Erentok, A.; Luljak, P. L.; Ziolkowski, R. W. Characterization of a Volumetric Metamaterial Realization of an Artificial Magnetic Conductor for Antenna Applications. *IEEE Trans. Antennas Propag.* **2005**, *53*, 160–172.
9. Kwon, D. H.; Werner, D. H. Low-Index Metamaterial Designs in the Visible Spectrum. *Opt. Express* **2007**, *15*, 9267–9272.
10. Choi, M.; Lee, S. H.; Kim, Y.; Kang, S. B.; Shin, J.; Kwak, M. H.; Kang, K.-Y.; Lee, Y.-H.; Park, N.; Min, B. A Terahertz Metamaterial with Unnaturally High Refractive Index. *Nature* **2011**, *470*, 369–373.
11. Huang, X. Q.; Lai, Y.; Hang, Z. H.; Zheng, H. H.; Chan, C. T. Dirac Cones Induced by Accidental Degeneracy in Photonic Crystals and Zero-Refractive-Index Materials. *Nat. Mater.* **2011**, *10*, 582–586.
12. Kocaman, S.; Aras, M. S.; McMillan, J. F.; Biris, C. G.; Panoiu, N. C.; Yu, M. B.; Kwong, D. L.; Stein, A.; Wong, C. W. Zero Phase Delay in Negative-Refractive-Index Photonic Crystal Superlattices. *Nat. Photonics* **2011**, *5*, 499–505.
13. Hao, J. M.; Yan, W.; Qiu, M. Super-Reflection and Cloaking Based on Zero Index Metamaterial. *Appl. Phys. Lett.* **2010**, *96*, 101109.
14. Mocella, V.; Cabrini, S.; Chang, A. S. P.; Dardano, P.; Moretti, L.; Rendina, I.; Olynick, D.; Harteneck, B.; Dhuey, S. Self-Collimation of Light over Millimeter-Scale Distance in a Quasi-Zero-Average-Index Metamaterial. *Phys. Rev. Lett.* **2009**, *102*, 133902.
15. Jiang, Z. H.; Gregory, M. D.; Werner, D. H. Experimental Demonstration of a Broadband Transformation Optics Lens for Highly Directive Multibeam Emission. *Phys. Rev. B* **2011**, *84*, 165111.
16. Ziolkowski, R. W. Propagation in and Scattering from a Matched Metamaterial Having a Zero Index of Refraction. *Phys. Rev. E* **2004**, *70*, 046608.
17. Litchinitser, N. M.; Maimistov, A. I.; Gabitov, I. R.; Sagdeev, R. Z.; Shalaev, V. M. Metamaterials: Electromagnetic Enhancement at Zero-Index Transition. *Opt. Lett.* **2008**, *33*, 2350–2352.
18. Antoniades, M. A.; Eleftheriades, G. V. A Broadband Series Power Divider Using Zero-Degree Metamaterial Phase-Shifting Lines. *IEEE Microwave Wireless Components Lett.* **2005**, *15*, 808–810.
19. Powell, D. A.; Kivshar, Y. S. Substrate-Induced Bianisotropy in Metamaterials. *Appl. Phys. Lett.* **2010**, *97*, 091106.
20. Ku, Z.; Brueck, S. R. Experimental Demonstration of Sidewall Angle Induced Bianisotropy in Multiple Layer Negative Index Metamaterials. *Appl. Phys. Lett.* **2009**, *94*, 153107.
21. Haupt, R. L.; Werner, D. H. *Genetic Algorithms in Electromagnetics*; Wiley: Hoboken, NJ, 2007.
22. Peterson, A. F.; Ray, S. L.; Mittra, R. *Computational Methods for Electromagnetics*; IEEE Press: Hoboken, NJ, 1998.
23. Weir, W. B. Automatic Measurement of Complex Dielectric-Constant and Permeability at Microwave-Frequencies. *Proc. IEEE* **1974**, *62*, 33–36.
24. Nicolson, A. M.; Ross, G. F. Measurement of Intrinsic Properties of Materials by Time-Domain Techniques. *IEEE Trans. Instrum. Meas.* **1970**, *19*, 377–382.
25. Smith, D. R.; Schultz, S.; Markos, P.; Soukoulis, C. M. Determination of Effective Permittivity and Permeability of Metamaterials from Reflection and Transmission Coefficients. *Phys. Rev. B* **2002**, *65*, 195104.
26. Leonhardt, U. Optical Conformal Mapping. *Science* **2006**, *312*, 1777–1780.
27. Schurig, D.; Mock, J. J.; Justice, B. J.; Cummer, S. A.; Pendry, J. B.; Starr, A. F.; Smith, D. R. Metamaterial Electromagnetic Cloak at Microwave Frequencies. *Science* **2006**, *314*, 977–980.
28. Pendry, J. B.; Holden, A. J.; Stewart, W. J.; Youngs, I. Extremely Low Frequency Plasmons in Metallic Mesostructures. *Phys. Rev. Lett.* **1996**, *76*, 4773–4776.
29. Pendry, J. B.; Holden, A. J.; Robbins, D. J.; Stewart, W. J. Magnetism from Conductors and Enhanced Nonlinear Phenomena. *IEEE Trans. Microwave Theory Tech.* **1999**, *47*, 2075–2084.
30. Drachev, V. P.; Chettiar, U. K.; Kildishev, A. V.; Yuan, H.-K.; Cai, W.; Shalaev, V. M. The Ag Dielectric Function in

Plasmonic Metamaterials. *Opt. Express* **2008**, *16*, 1186–1195.
31. Lepetit, L.; Chériaux, G.; Joffre, M. Linear Techniques of Phase Measurement by Femtosecond Spectral Interferometry for Applications in Spectroscopy. *J. Opt. Soc. Am. B* **1995**, *12*, 2467–2474.
32. Meshulach, D.; Yelin, D.; Silberberg, Y. White Light Dispersion Measurements by One- and Two-Dimensional Spectral Interference. *IEEE J. Quantum Electron.* **1997**, *33*, 1969–1974.
33. Wadsworth, W.; Joly, N.; Knight, J.; Birks, T.; Biancalana, F.; Russell, P. Supercontinuum and Four-Wave Mixing with Q-Switched Pulses in Endlessly Single-Mode Photonic Crystal Fibres. *Opt. Express* **2004**, *12*, 299–309.
34. Haus, H. A. *Waves and Fields in Optoelectronics*; Prentice-Hall: Upper Saddle River, NJ, 1984.